Micromechanics of magnetorheological suspensions

Eric M. Furst and Alice P. Gast*
Department of Chemical Engineering, Stanford University, Stanford, California 94305-5025
(Received 13 December 1999)

We apply optical trapping techniques in a magnetorheological (MR) suspension, allowing us to directly measure the mechanical properties of single dipolar chains, such as the rupturing tensions and strains under tensile and lateral deformations. Our results are in excellent agreement with calculations of the rupturing tensions using a self-consistent point dipole model of the particle interaction that accounts for induction and multibody effects along the chain. Additionally, we observe the annealing of chain defects under an applied stress, such as the inclusion of neighboring particles into the chain. The micromechanical properties of single chains offers important insight into magnetorheology and electrorheology, especially the yield stress behavior.

PACS number(s): 82.70.Dd

I. INTRODUCTION

The key to understanding and controlling the rheology of a colloidal system lies in characterizing the microstructure and its response to perturbation [1]. The formation of well-defined microstructures in a magnetorheological (MR) suspension offers a clear example. During the application of an external magnetic field to a MR suspension, the particles acquire dipole moments proportional to the field strength. When the dipolar interaction between particles exceeds thermal energy, the particles aggregate into chains of dipoles aligned in the field direction. Because energy is required to deform and rupture the chains, this microstructural transition is responsible for the onset of a large, ''tunable,'' finite yield stress. In fact, the ability of a MR system to elastically store energy on a slow time scale and viscously dissipate it on much faster time scales is common to other materials that exhibit a yield stress behavior, including the electrical analog of MR systems, electrorheological (ER) suspensions, as well as foams [2].

Until now, the ability to probe the microscopic mechanical properties of MR and ER materials has been limited to observation during the application of mechanical stresses [3], inferences from bulk rheological response during transient or oscillatory shear [4,5], and simulation techniques [2]. Our recent application of optical trapping techniques have allowed us to directly study the micromechanical properties of dipolar chains and chain aggregates in a MR suspension [6].

The application of optical trapping to MR suspensions is an extension of the microscopic manipulation and *in situ* force-sensing techniques that have led to significant insights in biomechanical, polymeric, and colloidal systems. A single-beam optical gradient force trap, or ''laser tweezer,'' was realized by Ashkin and co-workers and later used to manipulate colloidal particles and living cells [7–9]. Since then, the ability to probe forces on the order of piconewtons (pN) to subnanometer length scales using laser tweezers has led to direct measurements of the mechanics of motor proteins [10–12], the forces of transcription [13], thermal-scale forces in colloidal systems [14,15], and the elastic properties of polymers [16].

In this paper we present our studies of the micromechanical properties of dipolar chains and chain aggregates in MR suspensions. In Sec. II A we discuss our experimental materials and methods, including the details of our sample preparation and our optical trapping techniques. We present the mechanical properties of individual dipolar chains as shear and tensile stresses are applied in Secs. III C and III D, respectively. Our measurements of the rupture tension in both cases are in good agreement with particle interactions calculated from a self-consistent point-dipole model when the effects of a double-layer interaction are included. Lastly, in Sec. III E, we discuss the mechanics of chain defects and their influence on the micromechanical response of chains as well as their role in the mechanics of columns formed by lateral coalescence of single chains. We summarize the main points of this work in Sec. IV.

II. EXPERIMENT

A. MR suspensions

We use two model MR suspensions for this study, a monodisperse ferrofluid emulsion and superparamagnetic polystyrene spheres. The superparamagnetic behavior of the droplets and beads are both based on the presence of monodomain ($\sim$10 nm) iron oxide grains dispersed within the particles. In the absence of an external magnetic field, these domains are randomly aligned, and do not contribute to a net moment for the MR particle. When placed in a field **H**, the iron oxide grains partially align in the field direction and the droplet or bead i acquires a net dipole

$$\mathbf{m}_i = \frac{4}{3}\pi a^3 \mu_0 \chi \mathbf{H}, \tag{1}$$

where a and χ are the particle radius and susceptibility. Equation (1) is applicable at low fields, well below the magnetic saturation of the particle, and χ includes demagnetization effects, as discussed below. A pair of particles will then interact via an anisotropic dipolar potential

*Author to whom all correspondence should be addressed. Electronic address: alice@chemeng.stanford.edu

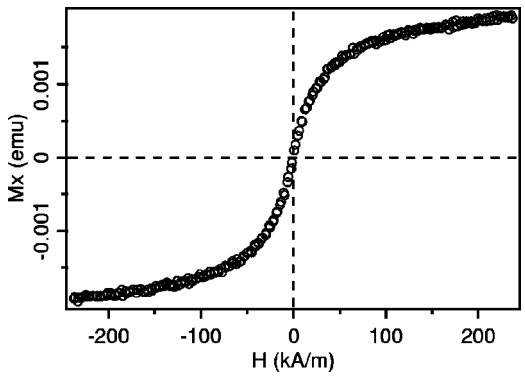

FIG. 1. The measured magnetization of our PS beads demonstrates the superparamagnetic behavior of the particles. The response of the particles is linear in the range of fields used here (<7600 A/m or 100 Gauss) with a measured susceptibility of $\chi = 0.67 \pm 0.1$.

$$U_{ij}^{dip} = \frac{1}{4\pi\mu_0} \frac{\mathbf{m}_i \cdot \mathbf{m}_j - 3(\hat{\mathbf{r}} \cdot \mathbf{m}_i)(\hat{\mathbf{r}} \cdot \mathbf{m}_j)}{r^3}. \tag{2}$$

$\mathbf{r}$ is the vector between particle centers and $\hat{\mathbf{r}}$ is the unit vector $\mathbf{r}/r$. The dipole strength characterizes the maximum interaction between two dipoles aligned tip-to-tail versus the thermal energy [17]

$$\lambda = -\frac{U_{ij}^{dip,max}}{kT} = \frac{\pi\mu_0 a^3 \chi^2 H^2}{9kT}. \tag{3}$$

When $\lambda \gg 1$, the dipolar interaction between particles is sufficiently strong to overcome Brownian motion, and chains of particles grow in the field direction.

The ferrofluid emulsion is synthesized following the fractionation method due to Bibette [18]. A mixture of ferrofluids (Ferrofluidics EMG 905 and EMG 909), composed of monodomain Fe_3O_4 particles suspended in a hydrocarbon, is emulsified into water using sodium dodecyl sulfate (SDS) (Sigma, cmc = 2.351 g/ml). The rough emulsion, consisting of particles between 0.1 and 10 μm in diameter, is fractionated through seven to nine successive depletion aggregations with SDS micelles. We vary the particle density by manipulating the ratio of the EMG 905 ($\rho = 1.24$ g/ml, $\chi_i = 1.9$, $M_{sat} = 400$ Gauss) and EMG 909 ($\rho = 1.02$ g/ml, $\chi_i = 0.8$, $M_{sat} = 200$ Gauss) ferrofluids. The final droplet susceptibility, accounting for the demagnetizing field for a sphere [19], $\chi = \chi_i/(1+\chi_i/3)$ is 0.86. The emulsion droplet density in this study is approximately $\rho = 1.1$ g/ml. We use particles of approximately 1.3 μm diameter.

For the second MR system, superparamagnetic polystyrene (PS) particles are acquired commercially (Bangs Laboratories, 38 wt% Fe_3O_4). From transmission electron microscopy (TEM) we find the particle size distribution spans diameters between 0.4 and 0.85 μm. The smallest particles are eliminated by removing the supernatant after allowing the largest and heaviest particles to settle. Our TEM images also reveal that the iron oxide distribution within particles is not always homogeneous—some particles show significant ''clumps'' within the polystyrene matrix. The average magnetic properties of the PS particles are measured using a vibrating sample magnetometer (VSM). As shown in Fig. 1, there is no observable hysteresis or remnant magnetization. The PS particle susceptibility χ over the range of fields used, 0 to 7600 A/m, is $\chi = 0.67 \pm 0.01$.

B. Optical trapping

Optical traps capable of holding and manipulating micron-sized dielectric particles are constructed simply by focusing a laser beam to a diffraction limited spot. In the ray-optic limit, the change in momentum of the converging beam as it is refracted through the particle imparts a force that pulls the particle into the region of highest intensity [20,21]. In addition to this gradient force, radiation pressure acts on the particle in the direction of the propagating beam. Using a high numerical aperture (NA) objective to create the trap ensures the largest possible intensity gradient to overcome the scattering force. Factors such as the incident intensity, particle geometry, laser wavelength and mode, particle refractive index relative to the surrounding medium, and beam polarization state contribute to the trapping force.

Our laser tweezers consist of two independently controlled traps. A single beam with transverse mode TEM_{00} from the 488 or 514 nm line of a 5W Ar^+ laser (Lexel Corporation) is expanded and passes through a polarizing cube splitter. The beams recombine to illuminate the back aperture of a $63\times$ NA 1.2 water immersion microscope objective (Zeiss C-Apochromat), creating two regions of highly focused light in our sample. The angle of incidence of each beam at the back aperture is controlled by a motorized gimbal mirror and 1:1 telescope, enabling us to move the traps two dimensionally throughout the entire focal plane. The sample-objective assembly is located at the center of Helmholtz coils. The intensity of each trap beam entering the objective can be as high as 25 mW depending on the desired trap stiffness and maximum trapping force. Images are captured on a charge-coupled device (CCD) camera (8 bit, 640 $\times$480 pixels), and stored with a S-VHS videorecorder (JVC BR-S622U) for further image processing and analysis (Scion Image).

Using the tweezers, force measurements on the order of 0.1 to 10 pN can be made by measuring the displacement of a particle from the trap center. The traps are calibrated for each experiment by measuring the displacement of a plain 3.5 μm PS bead held far from surrounding interfaces ($\gtrsim 50$ μm) while the sample stage is translated at known velocities U, thus imparting a drag force of $6\pi a\eta U$. The displacement of the bead is analyzed using particle tracking techniques [22], with a position sensitivity better than 30 nm. As mentioned above, the trap stiffness and maximum trapping force can be varied. Typical maximum trapping forces range between 3 and 12 pN [23].

Strong radiation pressure from scattering and absorption due to the presence of iron oxide grains in the MR particles prevents us from trapping them. Instead, we attach ''tethers'' that can then be held by the laser traps and used to deform the chains or measure applied tensions. For experiments using the ferrofluid emulsions, a small amount ($\phi < 10^{-6}$) of 3.5 μm streptavidin-coated beads are mixed with a similar volume fraction of 2.46 μm biotinylated superparamagnetic beads (39 wt% Fe_3O_4). Doublets that are formed through the strong streptavidin-biotin interaction ($K_a = 10^{15}$ M^{-1}) are

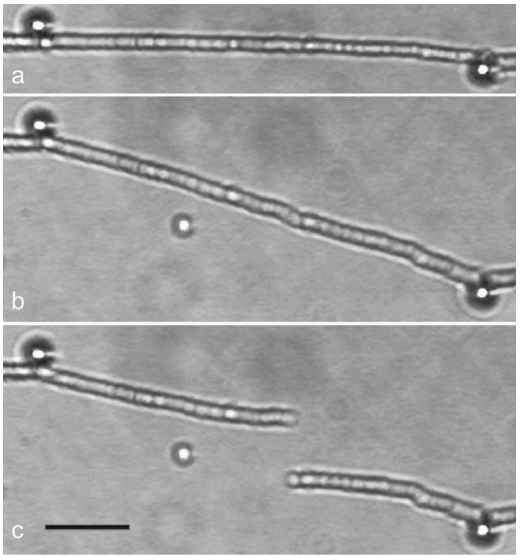

FIG. 2. Deformation of a dipolar chain of superparamagnetic emulsion droplets perpendicular to the applied field. Two 3.5 μm PS ''tethers'' are held in separate laser traps on the far left and right of the image. Attached to the tethers are biotinylated superparamagnetic PS particles that hold the emulsion chain. The right-most trap is translated down at 6 μm/s. (a) Before deforming the chain. (b) Immediately before the chain ruptures. (c) The chain recoils after rupturing. The scale bar is 10 μm.

physically incorporated into the emulsion chains and used to grab them with the laser traps. Thus, using the biotin-streptavidin interaction as an inert adhesive, we combine the PS tethers with magnetic ''handles'' capable of grabbing and manipulating particle chains. Streptavidin- and biotin-coated beads are obtained commercially (Bangs Laboratories) or produced in-house using straightforward covalent coupling chemistries for commercial carboxylated or amine-functionalized particles [24]. For experiments using the superparamagnetic PS particles, the entire MR suspension is biotinylated and mixed with the 3.5 μm streptavidin spheres ($\phi \approx 10^{-6}$).

Figure 2 illustrates a typical experimental geometry. The laser traps hold separate tethers that are attached to a dipolar chain aligned in the field direction. One trap is translated and deforms the chain perpendicularly or parallel to the applied magnetic field. The tension imparted on the chain is measured from the displacement of the second tether in the stationary trap. Translation rates are kept small ($\lesssim 6$ μm/s) to ensure accurate tension measurements and mechanical equilibrium.

III. RESULTS AND DISCUSSION

A. Particle interactions

Dipolar interaction. As described above, the unique reversible rheological transition MR suspensions exhibit is due to the superparamagnetic nature of the particles and the interaction of induced magnetic moments to form chains and chain aggregates. Equations (1) and (2) describe the interaction between field-induced moments; however, to understand the mechanics of dipolar chains, it is necessary to consider the effects of the local field due to chaining as well as the long-range interaction between particles. The field experienced by a dipolar particle i is due to the applied external field and the local field induced by a neighboring dipolar particle j, $\mathbf{H}_i = \mathbf{H}_0 + \mathbf{H}_j$, where

$$\mathbf{H}_j = \frac{1}{4\pi\mu_0} \frac{3\hat{\mathbf{r}}(\hat{\mathbf{r}}\cdot\mathbf{m}_j) - \mathbf{m}_j}{r^3}. \tag{4}$$

In a dipolar chain particle i experiences a total field due to all neighboring particles

$$\mathbf{H}_i = \mathbf{H}_0 + \sum_{j\neq i} \mathbf{H}_j. \tag{5}$$

The final form for the magnetic moment is

$$\mathbf{m}_i = \frac{4}{3}\pi a^3 \mu_0 \chi \left[\mathbf{H}_0 + \sum_{j\neq i} \frac{3\hat{\mathbf{r}}(\hat{\mathbf{r}}\cdot\mathbf{m}_j) - \mathbf{m}_j}{4\pi\mu_0 r^3} \right]. \tag{6}$$

Long-range particle interactions along the chain can be accounted for in a similar manner by summing over all particles interacting with particle i,

$$U_i^{dip} = \sum_{j\neq i} U_{ij}. \tag{7}$$

Equation (6) can be solved by numerical iteration to find self-consistent particle moments and interaction energies. Numerical calculations are useful for arbitrary particle configurations, such as chains with defects. An analytical solution to Eq. (6) is possible in the case of infinitely long linear chains. One can then find the particle moments self-consistently since $\mathbf{m}_i = \mathbf{m}_j$. Equation (6) is written as

$$\mathbf{m}_i = \frac{4}{3}\pi a^3 \mu_0 \chi \left[\mathbf{H}_0 + 2\sum_{n=1}^{\infty} \frac{3\hat{\mathbf{r}}(\hat{\mathbf{r}}\cdot\mathbf{m}_i) - \mathbf{m}_i}{4\pi\mu_0 (nr)^3} \right], \tag{8}$$

where $\mathbf{r}$ becomes the average interparticle spacing. Following Zhang and Widom [25] the sum in Eq. (8) is expressed in terms of the zeta function $\zeta(3) = \Sigma_{n=1}^{\infty}(1/n^3) \approx 1.202$. The components of $\mathbf{m}_i$ and subsequent interaction energy and force are then directly calculated. Summing the interactions for an infinite chain, the interaction between any two particles becomes

$$U^{dip} = \frac{m_i^2 \zeta(3)}{4\pi\mu_0} \left[\frac{1 - 3\cos^2\theta}{r^3} \right], \tag{9}$$

where θ is the angle of the chain. Calculations based on infinite chains are often a reasonable approximation since we measure mechanical properties far from the chain ends.

Double-layer interaction. Both the emulsion droplets and PS MR particles are electrostatically stabilized with an anionic surfactant. The repulsive double layer is included in our calculations of chain rupturing tensions using the Derjaguin approximation [26],

$$U^{el}(r) = 2\pi\epsilon\epsilon_0 \psi_0^2 a \ln[1 + e^{-\kappa(r-2a)}], \tag{10}$$

where ϵ is the dielectric permittivity of the suspending medium and κ is the inverse Debye screening length. $\kappa = 0.3$ nm^{-1} for the 2.35 g/L SDS solution. The surface po-

tential for PS particles due to SDS adsorption is $\psi_0 = 40$ mV [27], while the emulsion droplets have a surface potential of approximately 45 mV [28].

B. MR suspension rheology

The steady-shear rheological response of a MR suspension is typically described as a Bingham fluid with a shear stress

$$\tau = \eta_p \dot{\gamma} + \tau_0, \tag{11}$$

where η_p is the plastic viscosity, $\dot{\gamma}$ is the shear rate, and τ_0 is the Bingham or *dynamic yield stress* [29]. The shear stress typically increases as H_0^2 at low field strengths, similar to ER suspensions; however, at intermediate field strengths τ scales subquadratically [30–32]. At the highest field strengths τ becomes independent of H_0 and instead scales as $\sim M_{sat}^2$ [33]. η_p is generally insensitive to the applied field at large field strengths. The minimum stress required to induce flow in a MR suspension is not necessarily the Bingham stress but the *static yield stress* [2].

Microscopic models of the rheological properties of MR and ER systems, especially with respect to the dynamic and static yield stress behavior, focus on the response of the field-induced microstructure to deformation perpendicular to the field direction. Klingenberg and Zukoski [3] and Martin and Anderson [34] discuss chain models of electrorheology that capture the essential properties of the dynamic yield stress, including the quadratic field-dependence. Both are based on the calculated rupturing tension of dipolar chains with respect to imposed strain. The yield stress is then due to the collective rupturing and reformation of chains, which is applicable to dilute MR suspensions under low-field conditions and shear rates. In this regime the dipolar stress dominates the hydrodynamic stress and the structure consists largely of individual chains rather than columns or a dense, cross-linked network of chains. Bonnecaze and Brady have also confirmed the role of chain rupture with Stokesian dynamics simulations, and have shown that the dynamic yield stress is an inherent material property based on the disparity of time scales as chains slowly store energy elastically then rapidly dissipate it to the viscous medium [2]. Finally, Ginder and Davis also highlight the role of interparticle interactions and chain rupture, showing that the subquadratic behavior of τ with respect to H_0 at intermediate field strengths is due to local saturation of magnetization in the region of particle contacts [31].

C. Lateral deformation of single dipolar chains

Emulsion droplets. We measure the resistance of a single dipolar chain to a deformation perpendicular to the applied field. For instance, Fig. 2 shows lateral deformation and rupturing of an emulsion chain. Initially, the chain is aligned in the field direction. One trap is held stationary while the second is translated until the chain ruptures and recoils. The experiments are repeated for several dipole strengths, with excellent reproducibility. This is illustrated in Fig. 3 where the applied tension is plotted versus the strain for two sequential measurements of the same chain at $\lambda = 340$. As the data shows, the chain is initially held with zero applied tension and strain. As strain is induced with a translating trap, an increasing tension is applied to the chain. When the tension exceeds the interparticle force, calculated as $f = -\nabla(U^{dip} + U^{el})$ from Eqs. (9) and (10), the chain ruptures, shown by the arrow. The chains ''snap'' back into contact when they are brought sufficiently close, and the measurement is repeated, exhibiting essentially identical behavior.

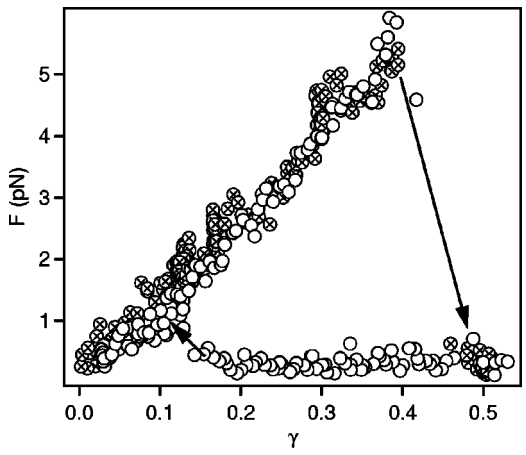

FIG. 3. Applied tension with respect to the imposed bending strain on a chain of dipolar emulsion droplets. The chain is initially deformed until rupturing at 5.5 pN (crossed circles). The right-most arrow indicates the drop in tension as the chain ruptures. For the second measurement (open circles) the chain halves are reassembled. The left-most arrow indicates the point at which the chain fragments ''jump'' back into contact. The second measurement demonstrates the reproducibility of the rupturing tension.

Figure 4 summarizes the measured rupture tensions versus the rupture strains for several dipole strengths. The average rupturing strains are 0.39, 0.37, and 0.33 for $\lambda = 340$, 240, and 150, respectively, from which we calculate the corresponding rupturing tensions of 5.7, 4.2, and 2.6 pN. The rupture tensions are in excellent agreement with values calculated from Eqs. (9) and (10). This highlights the importance of accounting for mutual induction between particles and chaining effects when considering the interactions in

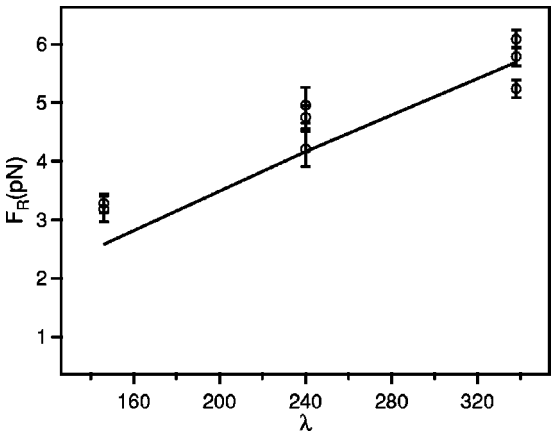

FIG. 4. Experimental (symbols) and calculated (line) results. Rupture tensions for chains of paramagnetic emulsion droplets deformed perpendicularly to the applied magnetic field at $\lambda = 150$, 240, and 340. The corresponding average rupture strains are 0.33, 0.37, and 0.39.

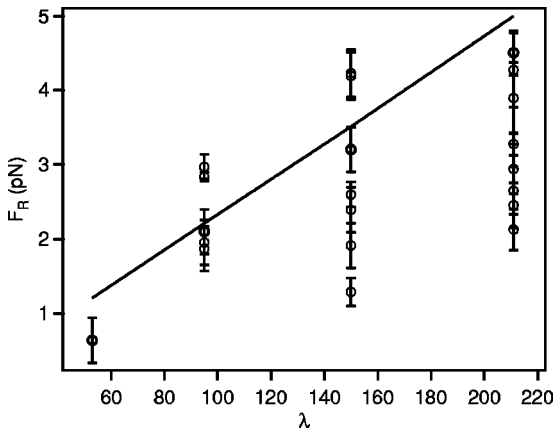

FIG. 5. Measured rupture tensions as a function of dipole strength for chains of magnetic PS beads deformed perpendicularly to the field direction. The presence of smaller particles in the PS system as well as heterogeneity of magnetite distribution within some particles creates weak points, causing them to rupture at lower applied tensions. The line indicates the calculated rupture tensions for 0.85 μm particles.

MR suspensions. It is also interesting to note that the presence of a double-layer interaction decreases the calculated rupture tension by $\sim 0.5-1$ pN.

PS particles. Figure 5 shows the rupture tensions as a function of λ. Calculations based on the nominal particle size, 0.85 μm, agree well with the upper bounds of our measured rupture tensions. As one would expect, the incorporation of smaller particles into the chains creates weaknesses that cause the chains to rupture at lower tensions. The lower bound of the measured rupture tensions correspond to particle diameters between 0.6 and 0.8 μm. Magnetic heterogeneity caused by the uneven distribution of iron oxide in some particles may also play a role in weakening the overall chain strength. The average rupture tensions, although lower than those expected from the nominal particle diameter, still increase with increasing dipole strength. They are 2.3 ± 0.5 pN, 2.6 ± 1.2 pN, and 3.1 ± 0.8 pN for $\lambda = 96$, 150, and 210, respectively.

Defects in the chains occur more readily in the PS system due to the polydispersity, an effect which can be seen in Fig. 6. The PS chains tend to deform unevenly, with ''steps'' of lower and higher field alignment, in contrast to Fig. 2.

While we show that individual chains can exhibit a wide range of rupture tensions even at the same dipole strength, the average mechanical properties of the chains are most

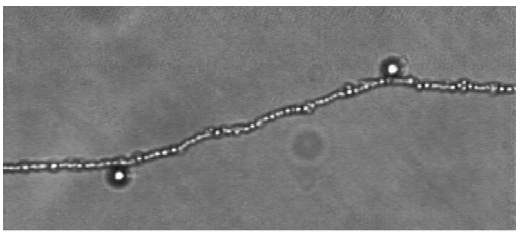

FIG. 6. A dipolar chain of PS particles deformed perpendicular to the field shows ''steps'' caused by defects. The defects stabilize short steep regions, allowing the larger segments in between to align in the field direction.

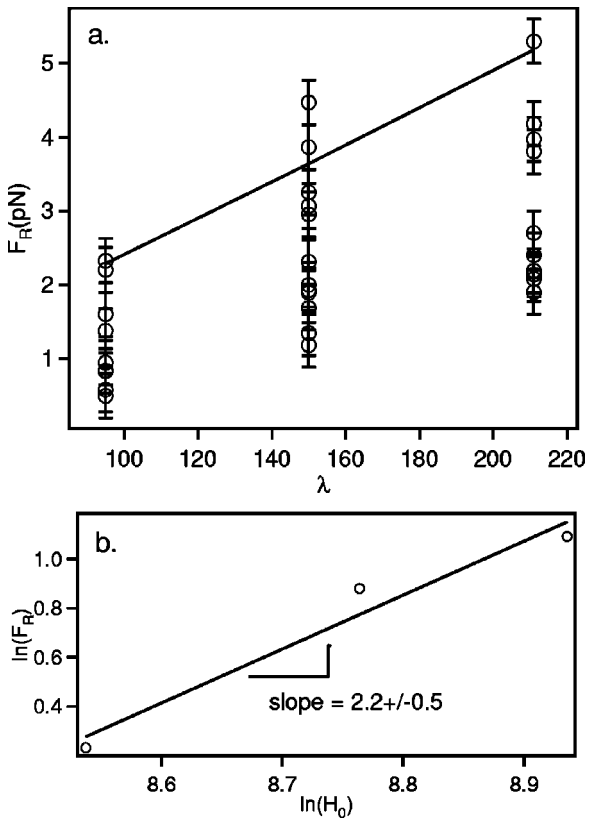

FIG. 7. Measured rupture tensions as a function of dipole strength for chains of magnetic PS beads extended in the field direction. (a) Defects and magnetic heterogeneity cause a broadening in the measured rupture tensions, similar to Fig. 5 compared with calculations for 0.85 μm particles. (b) The average rupture tensions increase roughly as the square of the applied field, indicating that magnetic saturation is not a factor.

useful for estimating the bulk rheological behavior. In a system of chains spanning two plates, for instance, the yield stress will be due to the deformation, rupturing, and subsequent reformation of a large number of chains when one of the plates is sheared. Considering this, the agreement between the experiments and the calculated rupturing tensions for both the emulsion and PS particles would result in the observed quadratic field dependence of the shear stress of MR and ER suspensions at low shear rates and volume fractions.

D. Deformation of dipolar chains in the field direction

In addition to lateral deformation, we apply tension to chains in the field direction to compare with our calculated rupturing tensions. Chains deformed along the field should rupture at somewhat higher tensions compared with the lateral deformation experiments since the interparticle interaction is strongest in the direction of the field.

Figure 7 illustrates the rupture tensions measured for chains of PS particles deformed in the field direction. These linear deformation experiments exhibit behavior analogous to the bending experiments of PS particles discussed above. Most notable is the large range of measured rupture tensions for each dipole strength. Like the bending experiments, this is due to the polydispersity. Again, the highest measured tensions agree well with calculated rupture tensions based on

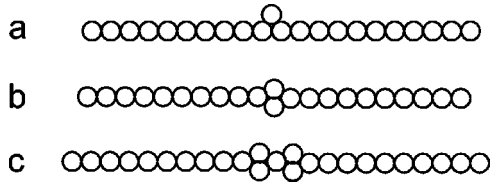

FIG. 8. Common defects observed in dipolar chains are characterized as (a) satellites, (b) cruciforms, and (c) double cruciforms.

the nominal particle size. The lowest forces measured are consistent with particle sizes on the order of 0.6 μm. The average rupture tensions are 1.3 ± 0.6 pN, 2.4 ± 1.0 pN, and 3.0 ± 1.1 pN for $\lambda=96$, 150, and 210, respectively.

Chains exhibit a slight increase in strain during linear deformation, typically under 0.05. Initially, the chains are fluctuating thermally [35], thus the contour length of the chain between tether points is longer than their separation distance. The observed strain increase is most likely due to the straightening of this contour length. The distance between the equilibrium and the rupturing particle separations is $\lesssim 0.05$ particle radii, and thus should not contribute significantly to the strain increase.

In our earlier paper [6] we reported interesting occurrences of sudden, large strain increases during the extension of dipolar chains, contrasting their typically rigid behavior. There we speculated that sufficiently high applied tensions may induce chain reorganizations, such as the incorporation of ''satellite'' particles attached to the side of the chain. We will discuss the mechanics of such defects and reorganizations in the following section.

E. Micromechanical properties of defects

Chain defects are interesting for their micromechanical behavior and have important implications in MR rheology, especially for transient flows. Chain defects such as satellite particles can occur and influence the behavior as chains are deformed. Figure 8 illustrates typical defects observed in dipolar chains, including satellites, cruciforms, and multiple cruciforms.

Experimental confirmation of the relationship between large strain increases and chain reorganizations are shown in Fig. 9. The double-cruciform defect, highlighted in the series of images, anneals as a linear tension is applied to the chain. First [9(a) and 9(b)] the left-most cruciform rotates to form a satellite defect. In 9(c) and 9(d) the right cruciform begins to rotate and completely anneals, leaving one satellite defect [9(e)]. As the translation of the moving trap continues, the last satellite defect incorporates itself into the chain through a rapid ''jump.'' After this last anneal [9(f)], the chain no longer deforms but ruptures instead as the tension increases. Figure 10 illustrates the measured tension during the defect annealing. As the strain is applied, the tension increases, but plateaus during the anneal at ~ 0.6 pN. After the anneal is complete, the tension increases rapidly to a final rupturing tension of 4.5 pN.

It is important to consider how defects affect the overall mechanics of chains as they are deformed. As the previous example illustrates, the annealing events can occur at a fairly low tension with respect to the final rupture tension. In this case, the anneal occurred at an applied tension of approximately 0.6 pN compared to a final rupture tension of 4.4 pN. We use quasistatic numerical calculations of chain rupturing to show that defects cause localized weaknesses in the

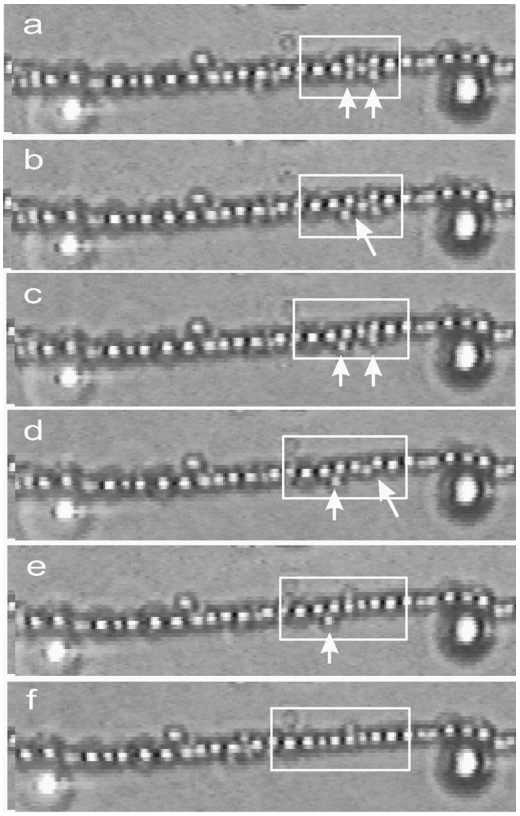

FIG. 9. Annealing a double cruciform defect during the application of tension to a dipolar PS chain. A white box highlights the chain strain increase during the annealing. The tension during the anneal is shown in Fig. 10. (a) Two arrows show the defects at the onset of the reorganization. (b) The top-most particle of the left cruciform rotates into the chain leading to a satellite/cruciform pair shown in (c). (d) The right cruciform is shown rotating into the chain. (e) The final satellite defect is shown before annealing. (f) After the final anneal, the chain is rigid and eventually ruptures.

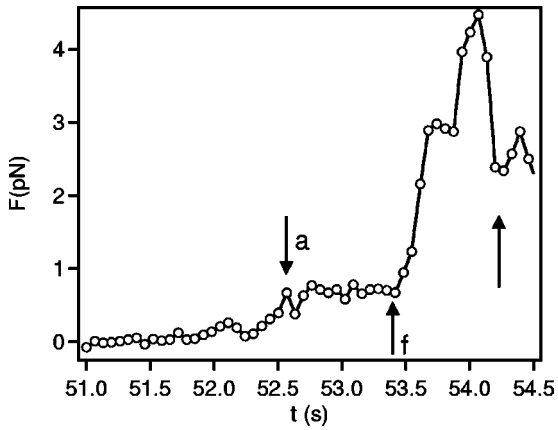

FIG. 10. The corresponding tension measured during the anneal of a double cruciform defect shown in Fig. 9; the letters refer to the first and last frames in the image sequence. The tension plateaus during the anneal at approximately 0.6 pN. The tension then increases rapidly and ruptures at 4.4 pN.

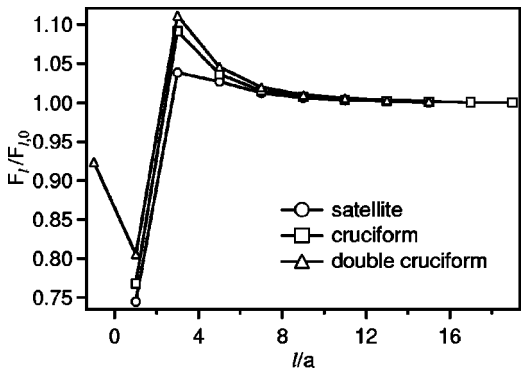

FIG. 11. The local mechanical properties caused by the presence of a defect at $l=0$. We plot the rupturing tension F_l normalized with the defect-free rupture tension $F_{l,0}$ as a function of distance l from a defect. A defect causes a localized weakness where chains are more likely to rupture or reorganize. Note for the double cruciform, $l=0$ corresponds to one of the defects. The point at $l=-1$ is the rupture tension between the defect and the center particle between the cruciforms.

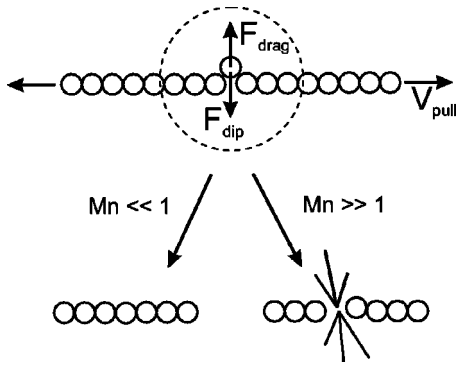

FIG. 12. Whether a chain ruptures or reorganizes at a defect depends on a balance of the dipolar interaction with the chain and the viscous drag, as characterized by the Mason number.

chain—points at which dipolar chains are more likely to rupture or reorganize.

The effects of several types of defects are examined using the finite-chain numerical calculations described in Sec. III A without implementing the double-layer interaction. A chain consisting of N particles with a satellite, cruciform, or double cruciform defect at the center is generated.

To calculate the local rupturing force we first select a point along the chain a distance l from the defect. The total energy

$$U_c=\sum_i \sum_{j>i} U_{ij}^{dip} \tag{12}$$

is computed as the chain is separated into two fragments by Δz along the chain axis at l. The rupturing force at point l is $F_l=-\partial U_c/\partial(\Delta z)$. During each numerical iteration of Δz we recalculate the particle moments before computing U_c.

In Fig. 11 we show F_l normalized with the defect-free rupture tension $F_{l,0}$ as a function of l for the three characteristic defects. The figure demonstrates that regions immediately adjacent to the defect rupture at lower tensions than a nondefective chain. This is not surprising, since the dipolar interactions near the defect are weak or unfavorable. For instance, the angle between a satellite particle and its nearest neighbors is 60°, which is in the repulsive regime of the dipolar interaction. The localization of this weakness is enhanced by the fact that distances along the chain immediately beyond the weak point are strengthened by the presence of a defect because they experience a larger number of favorable interactions compared with a perfect chain. With increasing distance from the defect, the rupturing force decays to the defect-free tension.

Whether a defect will cause the chain to rupture or rearrange while maintaining its integrity is dependent on several factors. For instance, consider a chain beginning to rupture at a satellite defect, shown in Fig. 12. As the chain fragments translate apart, two dominant forces are exerted on the satellite: the dipolar force that pulls the satellite into the expanding gap and the viscous resistance to this motion. The rate required to incorporate the particle into the chain to avoid rupturing is determined by the translational velocity of the separating chain fragments. Balancing the viscous force, characterized by the Peclet number Pe, with the dipolar force, yields the Mason number [3],

$$\mathrm{Mn}=\frac{\mathrm{Pe}}{\lambda}=\frac{54\eta V_{pull}}{\mu_0 a(\chi H_0)^2}, \tag{13}$$

where V_{pull} is the translational velocity of the chain fragments, determined by the velocity of the translating trap. Our experiments exhibit reorganizations at defects rather than ruptures because $\mathrm{Mn}\lesssim O(0.1)$.

Rearrangements in particle chains introduces a new mechanism for energy dissipation in MR and ER systems. As shown above it can significantly influence the rupturing tension of the particle chains depending on the imposed rate of deformation. The significance of small particle rearrangements have also been studied in transient and oscillatory shear experiments and simulations [4,5]. Parthasarathy and Klingenberg show that similar rearrangements in structures rather than the outright rupture of particle chains are responsible for the onset of nonlinear behavior in transient and oscillatory shear.

In [6] we report that particle rearrangements also play a role in the mechanical properties of columns of laterally aggregated single chains. For instance, at intermediate field strengths we find a *shear-hardening* behavior during which the column begins to deform, but acquires a more stable structure through reorganization of the particle configurations. Our previous work also shows that the formation of columns sufficiently increases the microstructural strength, which will dramatically influence the macroscopic yield stress. Understanding the lateral interactions that form columns [36–38] and their mechanical properties as the underlying suspension structures will significantly advance the ability of microscopic models to capture the rheology of MR and ER suspensions at higher volume fractions.

IV. CONCLUSIONS

In this paper we use laser trapping to study the micromechanical properties of a MR system that are of fundamental importance to the suspension rheology, especially with regards to the yield stress behavior. Single dipolar chains of

superparamagnetic particles are deformed parallel and perpendicular to the applied magnetic field. The rupturing tensions we measure are in excellent agreement with calculations based on a self-consistent point dipolar interaction that takes into account the mutual induction of particles as well as longer-ranged interactions along the chains. The quadratic behavior of the yield stress at low field strengths and volume fractions can therefore be identified with the force required to rupture individual chains. As we show, defects play important roles in the structure of chains and their micromechanical behavior. When bending chains, defects caused by size polydispersity cause ''steps'' of higher and lower field alignment. The rearrangement of defects provides an additional mechanism for energy dissipation other than full chain rupture. Defects also introduce localized weaknesses in chains where they are more likely to rupture or reorganize. We show that the tendency for defects to rupture versus reorganize is based on a balance between the force pulling the particle into an opening rupture versus the drag imparted on the particle, and can be characterized by the Mason number. Lastly, reorganizations may play an important role in the behavior of columns of chains, which are important in their own right for understanding the suspension rheology at higher particle volume fractions. It is clear that a detailed understanding the microscopic mechanics of dipolar chains and chain aggregates is fundamental to understanding magnetorheology and electrorheology.

ACKNOWLEDGMENTS

The authors would like to thank M. Fermigier for fruitful discussions and S. Chu and H. Babcock for their optical trapping expertise. Support by NASA (Grant No. NAG3-1887-1) is gratefully acknowledged.

[1] W. B. Russel, D. A. Saville, and W. R. Schowalter, *Colloidal Dispersions* (Cambridge University Press, New York, 1989).
[2] R. T. Bonnecaze and J. F. Brady, J. Rheol. **36**, 73 (1992).
[3] D. Klingenberg and C. Zukoski, Langmuir **6**, 15 (1990).
[4] M. Parthasarathy and D. J. Klingenberg, Rheol. Acta **34**, 417 (1995).
[5] M. Parthasarathy and D. J. Klingenberg, Rheol. Acta **34**, 430 (1995).
[6] E. M. Furst and A. P. Gast, Phys. Rev. Lett. **82**, 4130 (1999).
[7] A. Ashkin, Science **210**, 1081 (1980).
[8] A. Ashkin, J. M. Dziedzic, J. E. Bjorkholm, and S. Chu, Opt. Lett. **11**, 288 (1986).
[9] A. Ashkin, J. M. Dziedzic, and T. Yamane, Nature (London) **330**, 769 (1987).
[10] J. T. Finer, R. M. Simmons, and J. A. Spudich, Nature (London) **368**, 113 (1994).
[11] M. J. Schnitzer and S. M. Block, Nature (London) **388**, 386 (1997).
[12] K. Visscher, M. J. Schnitzer, and S. M. Block, Nature (London) **400**, 184 (1999).
[13] H. Yin *et al.*, Science **270**, 1653 (1995).
[14] A. Larsen and D. G. Grier, Nature (London) **385**, 230 (1997).
[15] J. Crocker, J. Matteo, A. Dinsmore, and A. Yodh, Phys. Rev. Lett. **82**, 4352 (1996).
[16] T. T. Perkins, D. E. Smith, R. G. Larson, and S. Chu, Science **268**, 83 (1995).
[17] A. Gast and C. Zukoski, Adv. Colloid Interface Sci. **30**, 153 (1989).
[18] J. Bibette, J. Colloid Interface Sci. **147**, 474 (1991).
[19] L. D. Landau and E. M. Lifshitz, *Electrodynamics of Continuous Media*, 2nd ed. (Pergamon, Oxford, 1984).
[20] A. Ashkin, Biophys. J. **61**, 569 (1992).
[21] K. Svoboda and S. M. Block, Annu. Rev. Biophys. Biomol. Struct. **23**, 247 (1994).
[22] J. C. Crocker and D. G. Grier, J. Colloid Interface Sci. **179**, 298 (1996).
[23] Our previous results with PS particles presented in Ref. [6] suffered from a systematic trap calibration error. The forces in that paper should be divided by a factor of 10. The disagreement between the corrected rupture tensions and our calculated values is resolved by directly measuring the magnetic properties of the paramagnetic PS beads. We find that the PS beads magnetize less than one would expect from the amount of iron oxide present, implying that not all of the iron oxide grains are free to reorient in the polymer matrix.
[24] *Covalent Coupling Protocols* (Bangs Laboratories, Inc., Fishers, IN).
[25] H. Zhang and M. Widom, Phys. Rev. E **51**, 2099 (1995).
[26] B. Derjaguin, Trans. Faraday Soc. **36**, 203 (1940).
[27] W. Brown and J. Zhao, Macromolecules **26**, 2711 (1993).
[28] F. L. Calderon *et al.*, Phys. Rev. Lett. **72**, 2959 (1994).
[29] R. G. Larson, *Structure and Rheology of Complex Fluids* (Wiley, New York, 1997).
[30] X. Tang and H. Conrad, J. Rheol. **40**, 1167 (1996).
[31] J. M. Ginder, Appl. Phys. Lett. **65**, 3410 (1996).
[32] J. Ginder, L. Davis, and L. Ellie, Int. J. Mod. Phys. B **10**, 3293 (1996).
[33] P. Phule and J. Ginder, Int. J. Mod. Phys. B **13**, 2019 (1999).
[34] J. E. Martin and R. A. Anderson, J. Chem. Phys. **104**, 4814 (1996).
[35] E. M. Furst and A. P. Gast, Phys. Rev. E **58**, 3372 (1998).
[36] T. C. Halsey and W. Toor, J. Stat. Phys. **61**, 1257 (1990).
[37] J. E. Martin, J. Odinek, T. C. Halsey, and R. Kamien, Phys. Rev. E **57**, 756 (1998).
[38] E. M. Furst, Ph.D. thesis, Stanford University, 2000 (unpublished).